ESI (Supplementary information)

Effects of A-site composition of perovskite ($Sr_{1-x}Ba_xZrO_3$) oxides on H atoms adsorption, migration, and reaction

Authors: Yuta Tanaka[1], Kota Murakami[1], Sae Doi[1], Kazuharu Ito[1], Koki Saegusa[1], Yuta Mizutani[1], Sasuga Hayashi[1], Takuma Higo[1], Hideaki Tsuneki[1], Hiromi Nakai[2] and Yasushi Sekine[1]

[1]Applied Chemistry, Waseda University, 3–4–1, Okubo, Shinjuku, Tokyo 169–8555, Japan

[2]Chemistry and Biochemistry, Waseda University, 3–4–1, Okubo, Shinjuku, Tokyo 169–8555, Japan

1. Theoretical predictions for H atom adsorption energies by DFT calculations

For the evaluation of H atoms adsorption energies over $Sr_{1-x}Ba_xZrO_3$, we carried out DFT calculations. The conditions and the procedures of the geometry optimizations were as mentioned in the main text. The constructed slab and bulk models are shown in Fig. S2 and Table S1. The obtained values of the H atom adsorption energies (E(H adsorption)) and the Bader charges of surface oxygen sites are summarized in Table S2.

2. Catalyst preparation

We prepared catalysts of 5 wt% ruthenium (Ru) loaded on $Sr_{1-x}Ba_xZrO_3$ (x=0.000, 0.0625, 0.125, 0.250, 0.375, 0.500) supports. The $Sr_{1-x}Ba_xZrO_3$ supports were synthesized using a complex polymerization method, which can circumvent the segregation of metal cations [s1]. In purified water, each metal cation was dispersed and complexed with citric acid, then the formed complexes were condensed and polyesterified with ethylene glycol. Here, the metal cations homogeneously existed

and were immobilized in the rigid polyester network. After that, the obtained products were calcined at low temperatures to decompose the network. We obtained blackish powder precursors with some carbons remaining. Finally, the carbonized blackish powders were calcined at high temperatures to decompose the residual carbon and to sinter the oxides.

Using the synthesized pure oxides, Ru was loaded using an impregnation method. Tris(acetylacetonato)ruthenium (III) ($Ru(acac)_3$) precursor and $Sr_{1-x}Ba_xZrO_3$ powders were added to acetone solvents, then the slurries were stirred and evaporated. To remove the ligands of the $Ru(acac)_3$, the prepared powders were pre-treated at 723 K for 2 h in the stream of H_2/Ar=1/1 (total 100 SCCM).

3. X-ray diffraction (XRD)

XRD patterns were recorded to confirm the crystalline structures of $Sr_{1-x}Ba_xZrO_3$ and to decide whether Sr^{2+} and Ba^{2+} can completely be incorporated into the perovskite-A-site. Figure S3 presents the obtained XRD patterns, indicating that $SrZrO_3$ can dissolve Ba^{2+} at any ratio (x). In addition, XRD measurements were also conducted for the fresh and the spent 5wt%Ru/$Sr_{1-x}Ba_xZrO_3$ catalysts to determine if the catalyst structure changed during activity tests. The recorded XRD patterns are shown in Fig. S4. The obtained XRD patterns exhibit that almost no peak shifts were observed between the fresh and the spent samples, which suggested that there are no significant changes in the catalyst structures during activity tests.

4. Effects of the A-site composition in $Sr_{1-x}Ba_xZrO_3$ oxide on the electronic state of loaded Ru

As explained in the main text, DFT calculations revealed the discontinuous change in the most stable exposed plane between the samples for $x \leq 0.50$ and $x \geq 0.75$. We presumed the difference in the exposed surface affected not only the H atom adsorption energies but also the electronic states of loaded Ru surface. We have previously reported that the high electron donating ability of the

catalyst supports made the Ru surface electron–rich, over which N_2H intermediate was stabilized [s2]. The stabilization of N_2H resulted in the enhancement of NH_3 synthesis activity in the electric field. In this investigation as well, the involvement of the Ru electronic state cannot be ignored. Thus, the impact of Sr^{2+}/Ba^{2+} ratio on the Ru electronic state was evaluated with CO–DRIFTS measurements and CO_2–TPD measurements.

4.1 *In–situ* DRIFTS measurements for adsorbed CO

To elucidate the effects of the A-site composition in $Sr_{1-x}Ba_xZrO_3$ on the electronic state of loaded Ru surface, the behavior of CO adsorbed over Ru were evaluated using diffuse reflectance infrared Fourier transform spectroscopy (DRIFTS) measurements. IR study of adsorbed CO is well–known as an effective method for probing the electronic state of loaded active metal surfaces because the CO stretching vibration energy is affected by the back–donation of electrons from an active metal [s3-s4]. This measurement was carried out using Fourier transform infrared spectrometer (FT–IR6200; Jasco Corp.) with a MCT detector and a DRIFTS reactor cell (DR–600Ai; Jasco Corp.) equipped with the ZnSe window. In advance of the measurements, all $Ru/Sr_{1-x}Ba_xZrO_3$ samples were pre–reduced at 723 K for 2 h under N_2/H_2=1/3 (total 60 SCCM) flow, then purged with Ar (60 SCCM) for 1 h to remove H species adsorbed on Ru surface. All the IR spectra were obtained at 303 K. First, the background–spectra were recorded under inert Ar (60 SCCM) atmosphere. Subsequently, 0.5%CO/Ar (60 SCCM) was supplied for 10 min. After the gas phase CO was purged with Ar, the *in–situ* spectra of adsorbed CO were recorded. All recorded spectra were obtained with 4.0 cm^{-1} resolution and 150 scans.

The results are shown in Fig. S5. The main peak was observed at around 2020–2050cm^{-1}, which derived from linearly adsorbed CO on Ru^0 surface [s5-s6]. Here, note that the behavior of adsorbed CO on Ru is too complicated owing to plenty of factors determining the peak position

including the electronic state, the particle size, the morphology of adsorbed site, and the CO coverage. As for our measurement in this paper, Ru particle sizes were almost identical among all catalysts (Table 1). Also, the difference of the CO coverage is negligible because Ru surface would be sufficiently covered with CO at 303 K. Therefore, the electronic state of Ru surface can be evaluated using the peak at around 2020–2050cm^{-1} shown in Fig. S5, which was assigned to linear CO adsorption on Ru^0. The results show the discontinuous peak shift of linear CO vibration toward lower wavenumber region for $x \geq 0.75$. This red-shift of the CO peak indicated that the electronic state of Ru became electron–rich. Based on this optical measurement and the most stable surface obtained by DFT calculations, it was assumed that the discontinuous shift of the CO peaks reflected the change in the exposed surface.

4.2 Basicity of $Sr_{1-x}Ba_xZrO_3$ supports evaluated by CO_2–TPD

As shown in the former section, the electronic state of Ru was discontinuously changed along with the increment in the Ba^{2+} content (x) in $Sr_{1-x}Ba_xZrO_3$. It is generally known the electron-donating ability is correlated to the basicity of an oxide surface [s7-s11]. Therefore, we conducted temperature–programmed desorption measurements of CO_2 (CO_2–TPD) to evaluate the basic properties of $Sr_{1-x}Ba_xZrO_3$ surfaces.

Before the adsorption of CO_2, each support 300 mg was pre–reduced at 723 K for 2 h in a stream of N_2/H_2=1/3 (240 SCCM), then purged with He (50 SCCM) for 1 h. After that, the sample was cooled down to 333 K, and 10%CO_2/He (50 SCCM) was fed for 1 h. The gas phase CO_2 was purged with He (50 SCCM) for 0.5 h. Afterwards, the sample was heated at a ramping rate of 3 K min^{-1} to 1073 K under He (50 SCCM) flow, and the CO_2 desorption profiles were detected. Quadrupole mass spectrometer (QGA; Hiden Analytical Ltd.) was used to monitor the desorbed CO_2 (m/z=44) and inert He (m/z=4).

The results of CO_2–TPD are shown in Fig. S6. From the TPD profiles, two main peaks were identified at around 650 K and at above 900 K. They were derived from the weak and the strong base sites on oxide surfaces, respectively. Moreover, we confirmed a discontinuous change in the support basicity. Little change in the intensity and the amounts of base sites over $Sr_{1-x}Ba_xZrO_3$ was observed for $x \leq 0.50$, whereas both of the two factors drastically increased for $x \geq 0.75$. In conclusion, it was clarified that the change in the basicity of catalyst supports caused the discontinuous trend in the electronic state of Ru for $x \geq 0.75$. Therefore, we performed other investigations using the samples in the range of $0.00 \leq x \leq 0.50$.

5. X–ray photoelectron spectroscopy (XPS)

XPS measurements were performed to evaluate the amount of hydroxy (OH) groups over $Sr_{1-x}Ba_xZrO_3$ (x=0.000, 0.250, 0.500) oxides. The obtained C1*s* and O1*s* spectra are shown in Figs. S7 and S8, the calculated OH ratios are summarized in Fig. S9 and Table S3. Furthermore, we also analyzed the XPS spectra obtained with the fresh and the spent 5wt%Ru/$SrZrO_3$ samples in order to confirm the change in the catalyst surface structures during the activity tests. The recorded C1*s*, O1*s*, Ru3*d*, Zr3*d*, Sr3*p*, and Sr3*d* spectra are shown in Fig. S12. As there were no significant differences in the spectral shapes between the fresh and the spent samples, we concluded that the catalyst surface structure did not change during the catalysis.

6. Activity tests

Temperature dependence for NH_3 synthesis rates in the electric field was investigated using 5wt%Ru/$Sr_{1-x}Ba_xZrO_3$ ($0.000 \leq x \leq 0.500$) catalysts. The experimental conditions are the same as the flow described in the main part. The results are represented in Fig. S10, the details in Tables S4 through S9. Furthermore, turn-over frequencies (TOF) were also calculated for the evaluation of catalytic

performances, summarized in Table 1 in the main part.

7. Distributions of the loaded Ru particle sizes (FE-TEM)

The loaded Ru particles over $Sr_{1-x}Ba_xZrO_3$ supports were analyzed with FE-TEM images. The obtained images and the histograms of the Ru particle size distributions are shown in Fig. S11.

8. Specific surface areas of catalysts

Among the most influential factors determining the particle size distributions of loaded Ru is a specific surface area (SSA) of catalyst supports. Therefore, we evaluated the SSA values of $Sr_{1-x}Ba_xZrO_3$ supports with BET method. The SSA values obtained with each support, summarized in Table 1 in the main text, tended to slightly increase in a higher Ba^{2+} content (x) region. Nevertheless, no correlation between the SSA values and the obtained Ru particle sizes was observed. In addition, the trend of TOFs was in close agreement with that of NH_3 synthesis rates. Therefore, we concluded that the small change in the SSA values had little effect on the catalytic performances. Moreover, we compared the SSA values of the fresh and the spent 5wt%Ru/$Sr_{1-x}Ba_xZrO_3$ catalysts, summarized in Table S10. The obtained SSA values were little altered after the activity tests, indicating the catalyst structures hardly changed during the NH_3 synthesis reaction in the electric field.

Notes and References

[s1] M. Kakihara and M. Yoshimura, *Bull. Chem. Soc. Jpn.*, 1999, **72**, 1427-1443.

[s2] K. Murakami, Y. Tanaka, S. Hayashi, R. Sakai, Y. Hisai, Y. Mizutani, A. Ishikawa, T. Higo, S. Ogo, J. G. Seo, H. Tsuneki, H. Nakai and Y. Sekine, *J. Chem. Phys*., 2019, **151**, 064708.

[s3] T. N. Ye, J. Li, M. Kitano, M. Sasase and H. Hosono, *Chem. Sci*., 2016, **7**, 5969–5975.

[s4] Z. Luo, Z. Zheng, L. Li, Y. T. Cui and C. Zhao, *ACS Catal*., 2017, **7**, 8304‑8313.

[s5] H. W. Chen, Z. Zhong and J. M. White, *J Catal*., 1984, **90**(1), 119‑126.

[s6] S. Y. Chin, C. T. Williams and M. D. Amiridis, 2006, *J*. *Phys*. *Chem*. *B*, **110**(2), 871‑882.

[s7] K. Aika, T. Takano and S. Murata, *J*. *Catal*., 1992, **136**(1), 126–140.

[s8] Z. Wang, B. Liu and J. Lin, *Appl*. *Catal*. *A*, 2013, **458**, 130–136.

[s9] Z. Wang, J. Lin, R. Wang and K. Wei, *Catal*. *Commun*., 2013, **32**(5), 11–14.

[s10] K. Sato, K. Imamura, Y. Kawano, S. Miyahara, T. Yamamoto, S. Matsumura and K. Nagaoka, *Chem*. *Sci*., 2017, **8**, 674–679.

[s11] K. Okura, K. Miyazaki, H. Muroyama, T. Matsui and K. Eguchi, *RSC Adv*., 2018, **8**, 32102–32110.

[s12] A. M. Glazer, *Acta*. *Crystallogr*. *Sect*. *B,* 1972, **28**, 3384.

[s13] A. M. Glazer, *Acta*. *Crystallogr*. *Sect*. *A*, 1975, **31**, 756.

Caption for Figures and Tables

Figure S1 A schematic image of the activity test reactor.

Figure S2 Atomic images of the optimized slab models of $Sr_{1-x}Ba_xZrO_3$ for (a) x=0.00, (b) x=0.25, (c) x=0.50, (d) x=0.75, and (e) x=1.00. The images above are from the side, and the ones below are from the top. Sr atoms are shown in orange, Ba in blue, Zr in green, and O in red.

Figure S3 XRD patterns (a) and the calculated lattice parameters (b) of the prepared $Sr_{1-x}Ba_xZrO_3$ ($0.000 \leq x \leq 0.500$) samples. The focused peaks in (a) are diffracted from (112), (200), and (020) plane.

Figure S4 XRD patterns (a) and the calculated cell volumes (b) for the fresh and the spent catalysts of 5wt%Ru/ $Sr_{1-x}Ba_xZrO_3$ ($0.000 \leq x \leq 0.500$) catalysts.

Figure S5 *In-situ* DRIFTS spectra obtained by the linear CO adsorbed on $Ru/Sr_{1-x}Ba_xZrO_3$ surfaces for x=0.00, 0.25, 0.50, 0.75, and 1.00.

Figure S6 Profiles for the temperature-programmed desorption of CO_2 over $Sr_{1-x}Ba_xZrO_3$ oxide surfaces for x=0.00, 0.25, 0.50, 0.75, and 1.00.

Figure S7 C1*s* X-ray photoelectron spectra with $Sr_{1-x}Ba_xZrO_3$ oxides pre-reduced at 723 K for 2 h under N_2/H_2=1/3 (240 SCCM) flow, (a) x=0.000, (b) x=0.250, and (c) x=0.500.

Figure S8 O1*s* X-ray photoelectron spectra with $Sr_{1-x}Ba_xZrO_3$ oxides pre-reduced at 723 K for 2 h under N_2/H_2=1/3 (240 SCCM) flow, (a) x=0.000, (b) x=0.250, and (c) x=0.500.

Figure S9 The hydroxy groups (OH) ratio over $Sr_{1-x}Ba_xZrO_3$ oxides (x=0.000, 0.250, and 0.500) calculated by C1*s* and O1*s* X-ray photoelectron spectra.

Figure S10 Temperature dependence for NH_3 synthesis rates in the electric field (0.1 MPa, 6.0 mA) using $5wt\%Ru/Sr_{1-x}Ba_xZrO_3$ ($0.000 \leq x \leq 0.500$) catalysts.

Figure S11 FE-TEM images and the obtained histograms of the $5wt\%Ru/Sr_{1-x}Ba_xZrO_3$ catalysts for (a) x=0.00, (b) x=0.063, (c) x=0.125, (d) x=0.250 (e) x=0.375, and (f) x=0.500.

Figure S12 X-ray photoelectron spectra obtained with the fresh and the spent 5wt%Ru/$SrZrO_3$ samples, (a) O1*s*, (b) C1*s*, Ru3*d*, and Sr3*p*, (c) Zr3*d*, and (d) Sr3*d*.

Table S1 The summary for the constructed bulk and slab models of $Sr_{1-x}Ba_xZrO_3$ ($0.00 \leq x \leq 1.00$). The lattice parameters of the $BaZrO_3$ cubic oxide (*Pm-3m*) were converted using the following equation, $a' = \sqrt{2}a$, $b' = \sqrt{2}b$, and $c' = 2c$

Table S2 The summary for the H atom adsorption energies (*E*(H adsorption)) and the surface oxygen Bader charges over $Sr_{1-x}Ba_xZrO_3$ (x=0.00, 0.25, and 0.50) surfaces

Table S3 The summary for the quantitative analysis of OH groups with O1*s* XPS spectra

Table S4 NH_3 synthesis rate over 5wt%Ru/$SrZrO_3$ in the electric field (0.1 MPa, 6.0 mA)

Table S5 NH_3 synthesis rate over 5wt%Ru/$Sr_{0.937}Ba_{0.063}ZrO_3$ in the electric field (0.1 MPa, 6.0 mA)

Table S6 NH_3 synthesis rate over 5wt%Ru/$Sr_{0.875}Ba_{0.125}ZrO_3$ in the electric field (0.1 MPa, 6.0 mA)

Table S7 NH_3 synthesis rate over 5wt%Ru/$Sr_{0.750}Ba_{0.250}ZrO_3$ in the electric field (0.1 MPa, 6.0 mA)

Table S8 NH_3 synthesis rate over 5wt%Ru/$Sr_{0.625}Ba_{0.375}ZrO_3$ in the electric field (0.1 MPa, 6.0 mA)

Table S9 NH_3 synthesis rate over 5wt%Ru/$Sr_{0.500}Ba_{0.500}ZrO_3$ in the electric field (0.1 MPa, 6.0 mA)

Table S10 Specific surface areas of the fresh and the spent 5wt%Ru/$Sr_{1-x}Ba_xZrO_3$ ($0.000 \leq x \leq 0.500$) catalysts

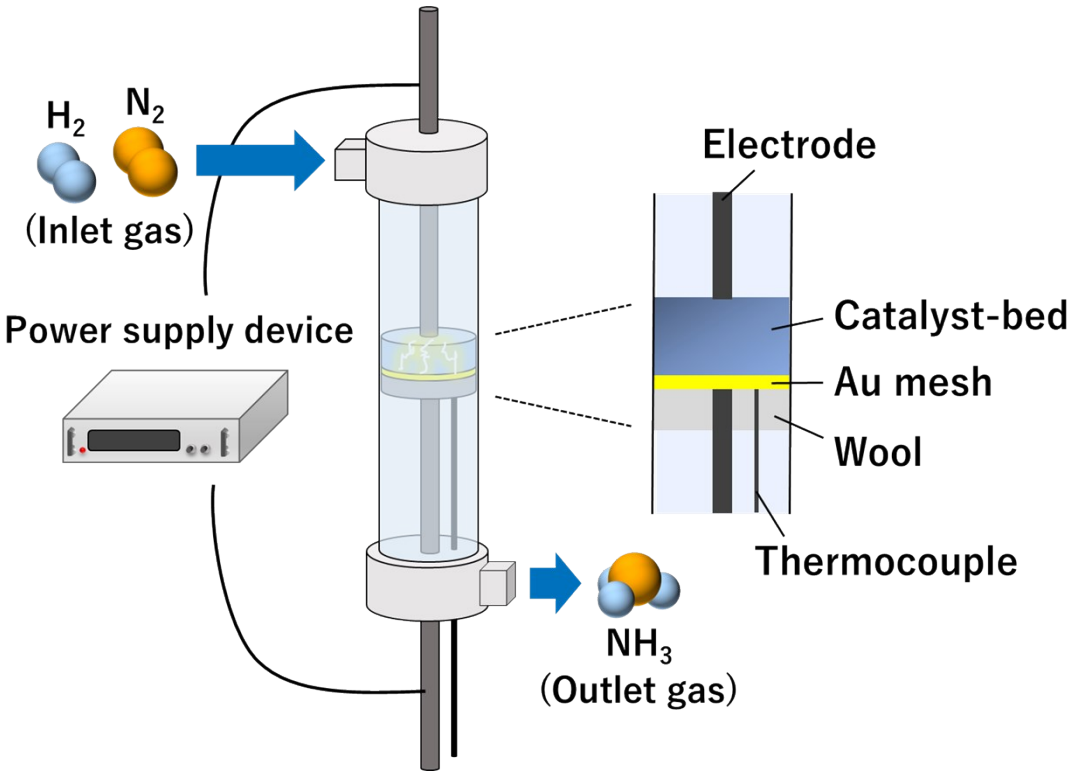

Figure S1 A schematic image of the activity test reactor.

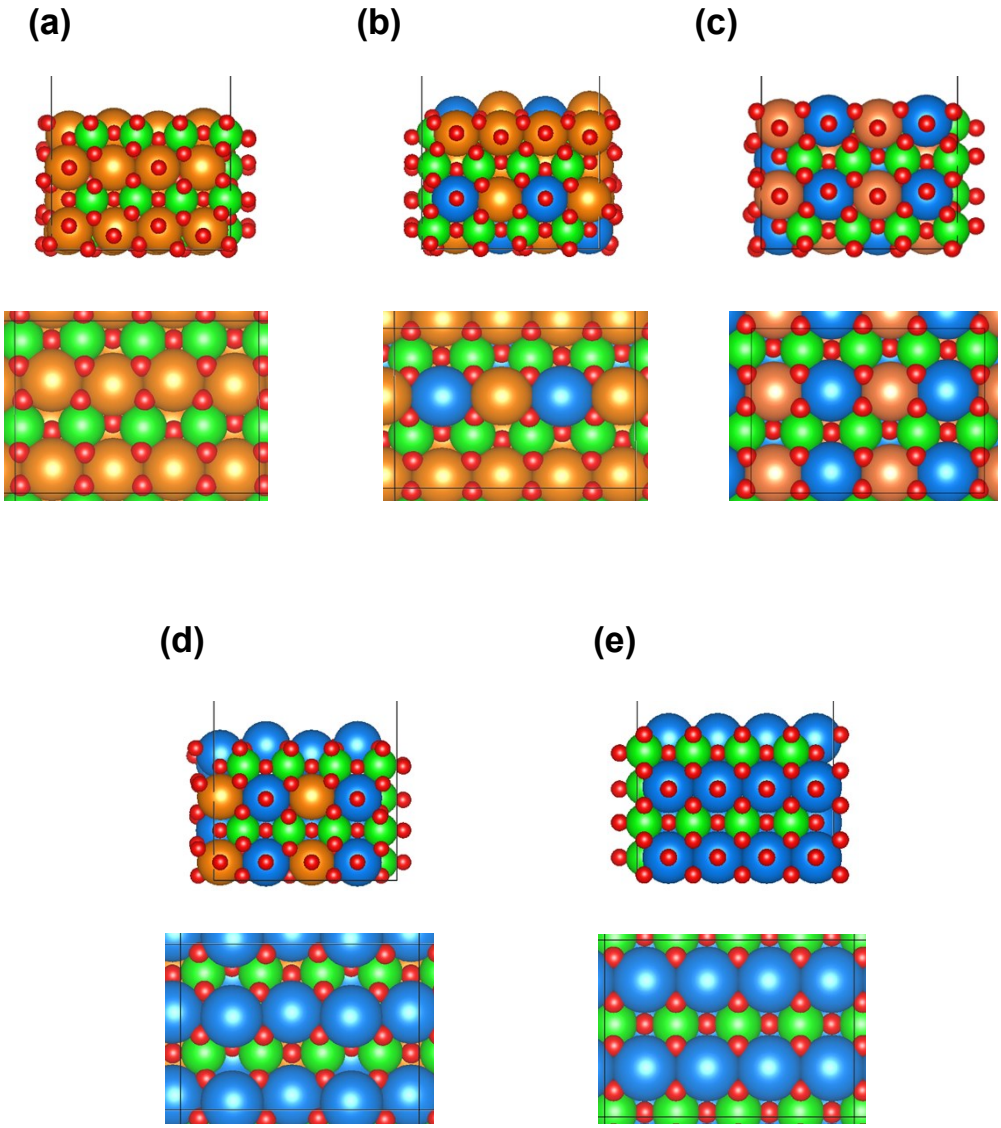

Figure S2 Atomic images of the optimized slab models of $Sr_{1-x}Ba_xZrO_3$ for (a) x=0.00, (b) x=0.25, (c) x=0.50, (d) x=0.75, and (e) x=1.00. The images above are from the side, and the one below are from the top. Sr atoms are shown in orange, Ba in blue, Zr in green, and O in red.

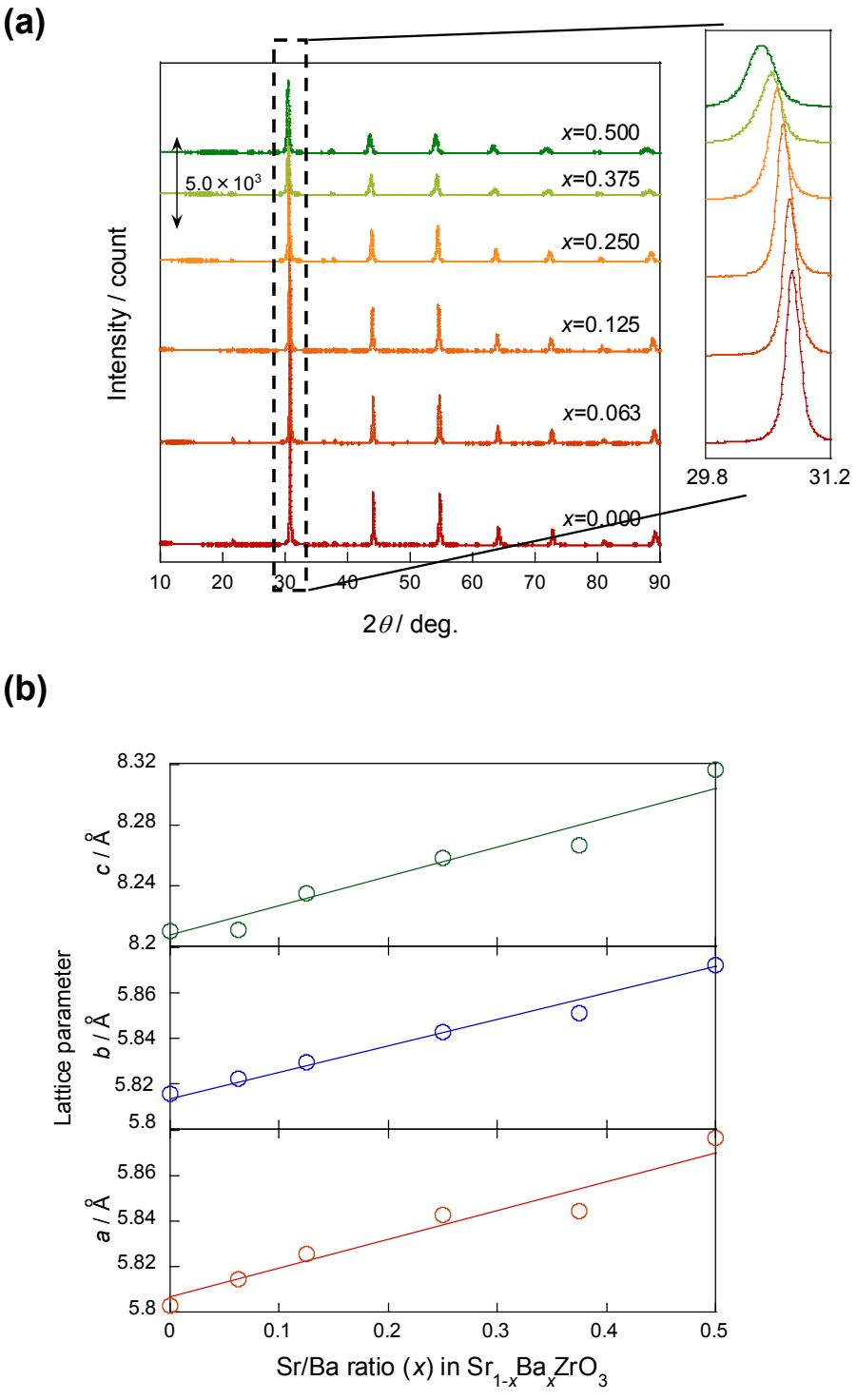

Figure S3 XRD patterns (a) and the calculated lattice parameters (b) of the prepared $Sr_{1-x}Ba_xZrO_3$ ($0.000 \leq x \leq 0.500$) samples. The focused peaks in (a) are diffracted from (112), (200), and (020) plane.

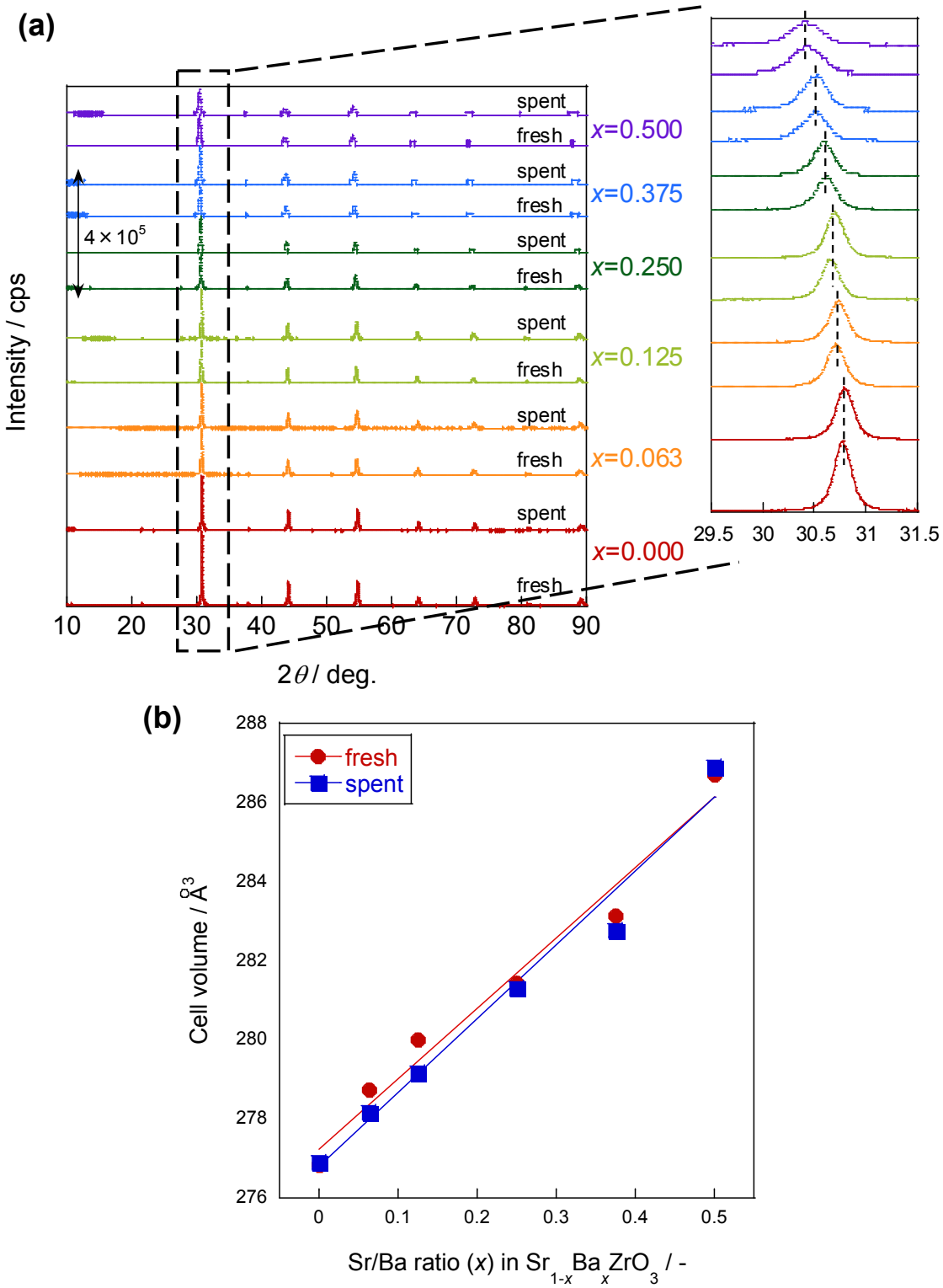

Figure S4 XRD patters (a) and the calculated cell volumes (b) for the fresh and the spent catalysts of 5wt%Ru/$Sr_{1-x}Ba_xZrO_3$ ($0.000 \leq x \leq 0.500$) catalysts.

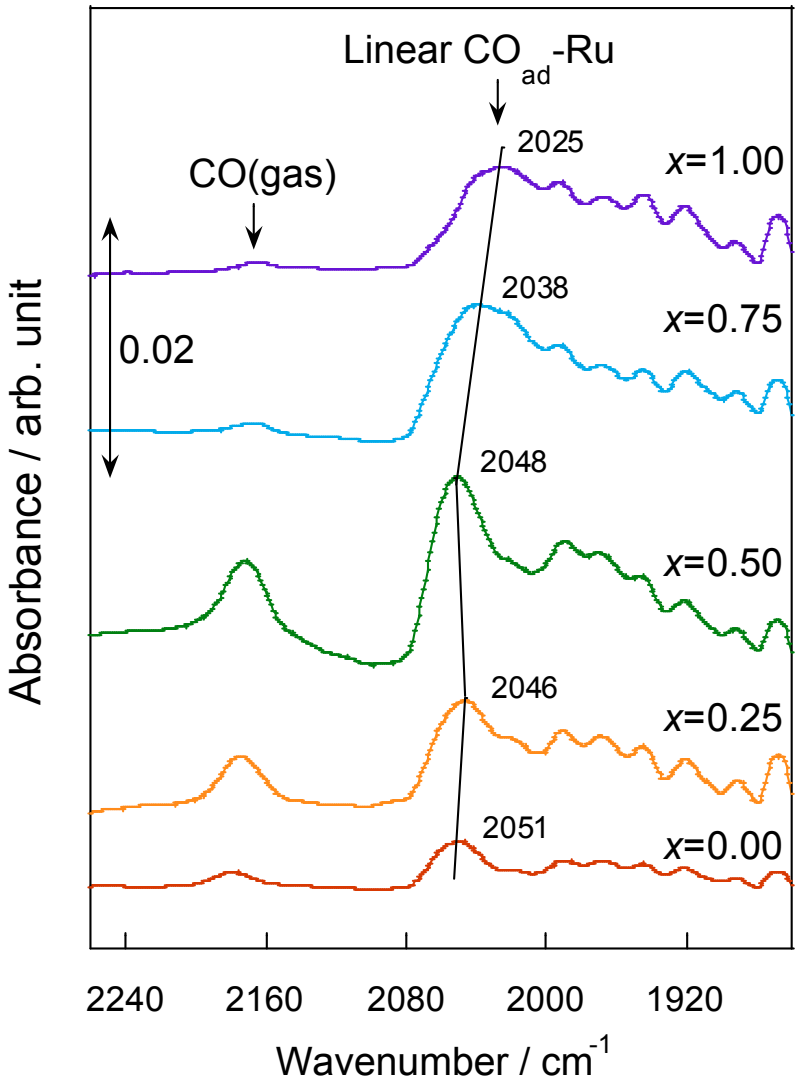

Figure S5 *In-situ* DRIFTS spectra obtained by the linear CO adsorbed on $Ru/Sr_{1-x}Ba_xZrO_3$ surfaces for x=0.00, 0.25, 0.50, 0.75, and 1.00.

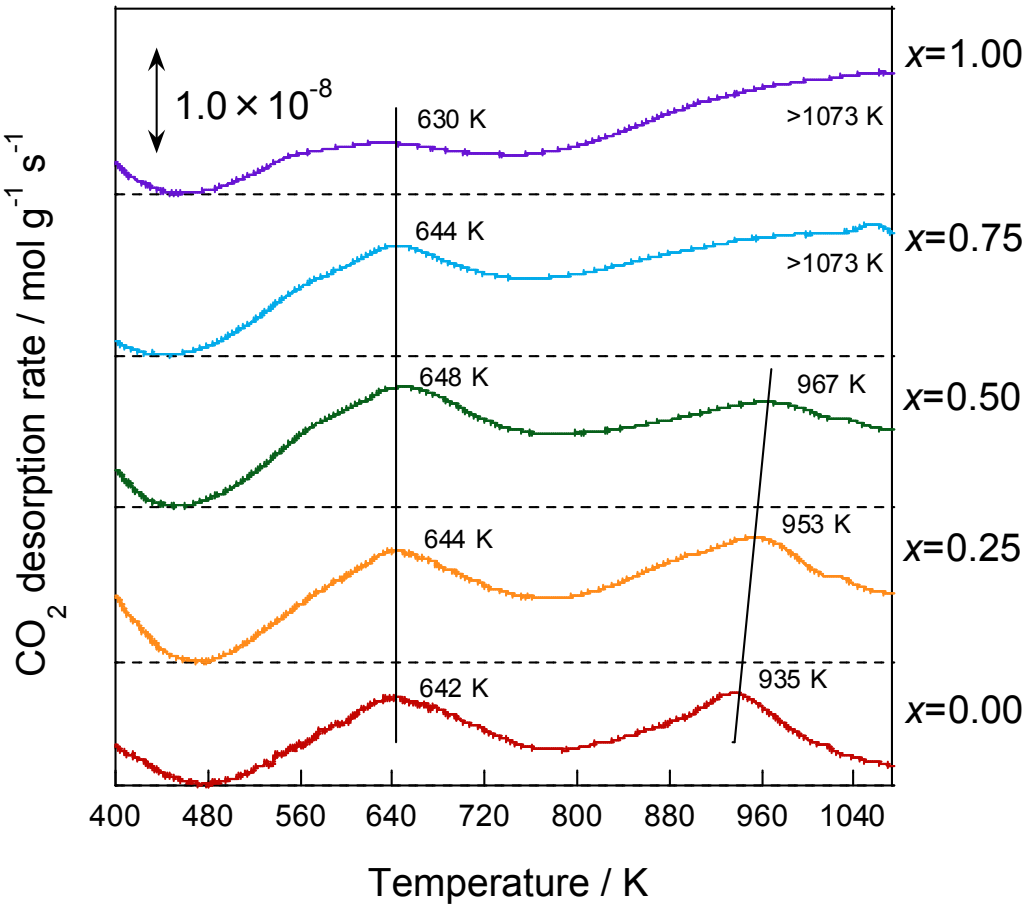

Figure S6 Profiles for the temperature-programmed desorption of CO_2 over $Sr_{1-x}Ba_xZrO_3$ oxide surfaces for x=0.00, 0.25, 0.50, 0.75, and 1.00.

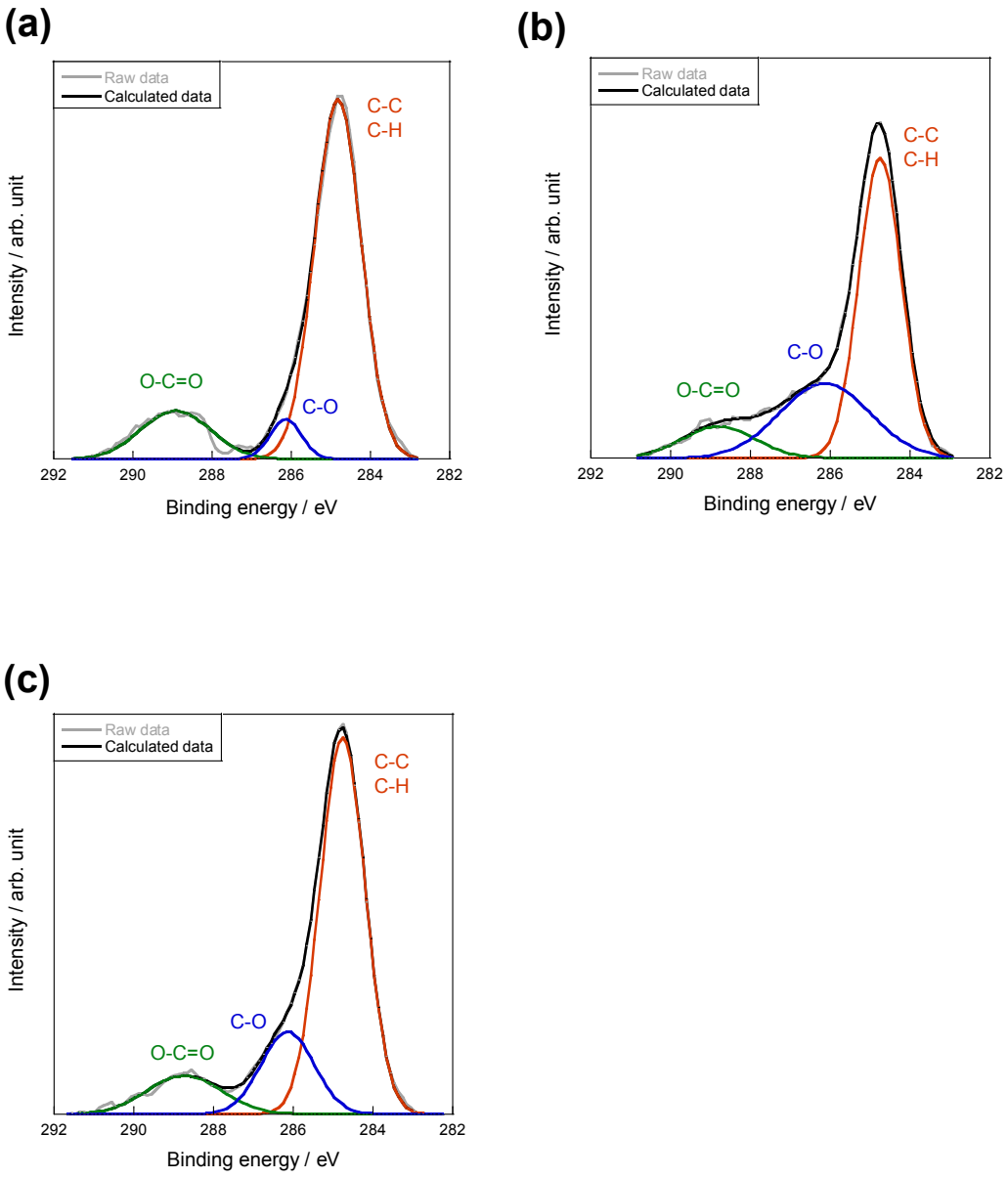

Figure S7 C1*s* X-ray photoelectron spectra with $Sr_{1-x}Ba_xZrO_3$ oxides pre-reduced at 723 K for 2 h under N_2/H_2=1/3 (240 SCCM) flow, (a) x=0.000, (b) x=0.250, and (c) x=0.500.

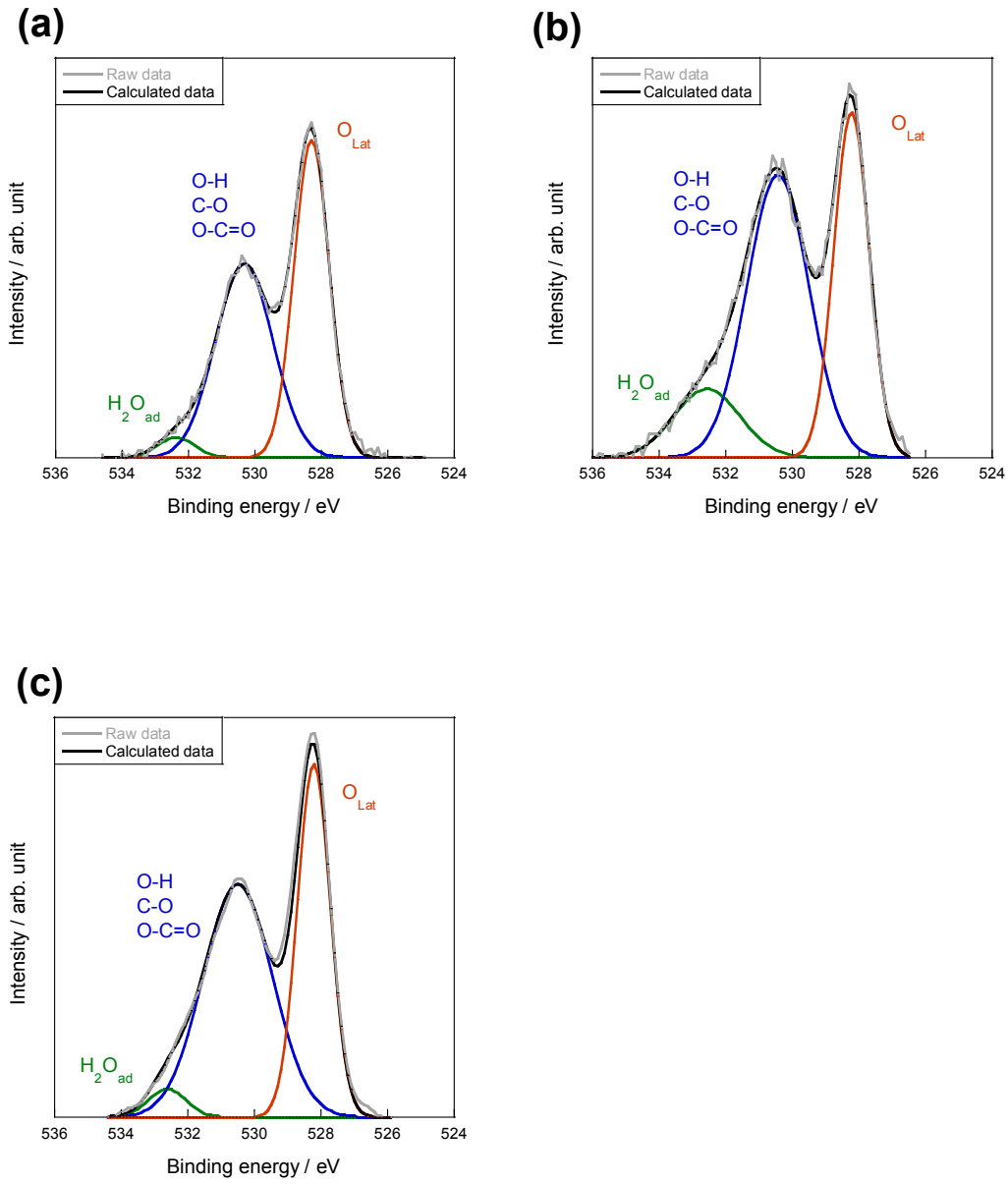

Figure S8 O1*s* X-ray photoelectron spectra with $Sr_{1-x}Ba_xZrO_3$ oxides pre-reduced at 723 K for 2 h under N_2/H_2=1/3 (240 SCCM) flow, (a) x=0.000, (b) x=0.250, and (c) x=0.500.

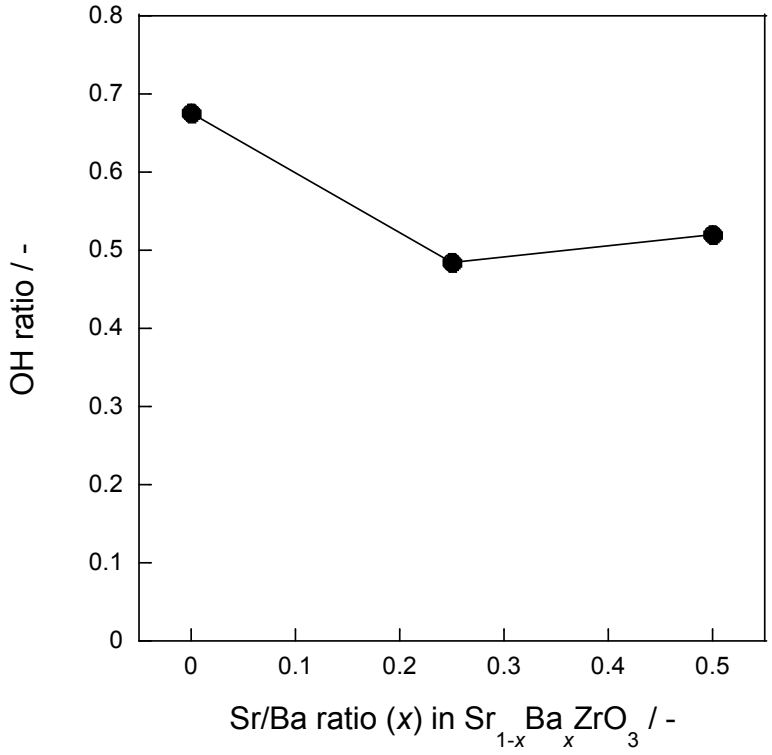

Figure S9 The hydroxy groups (OH) ratio over $Sr_{1-x}Ba_xZrO_3$ oxides (x=0.000, 0.250, and 0.500) calculated by C1*s* and O1*s* X-ray photoelectron spectra.

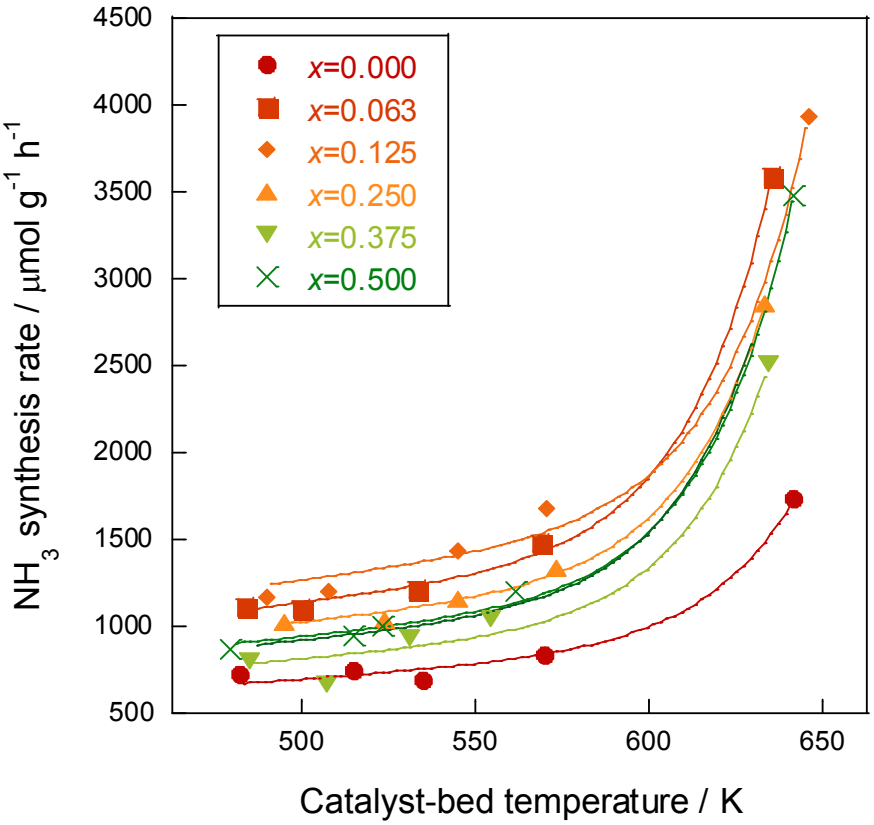

Figure S10 Temperature dependence for NH_3 synthesis rates in the electric field (0.1 MPa, 6.0 mA) using 5wt%Ru/$Sr_{1-x}Ba_xZrO_3$ ($0.000 \leq x \leq 0.500$) catalysts.

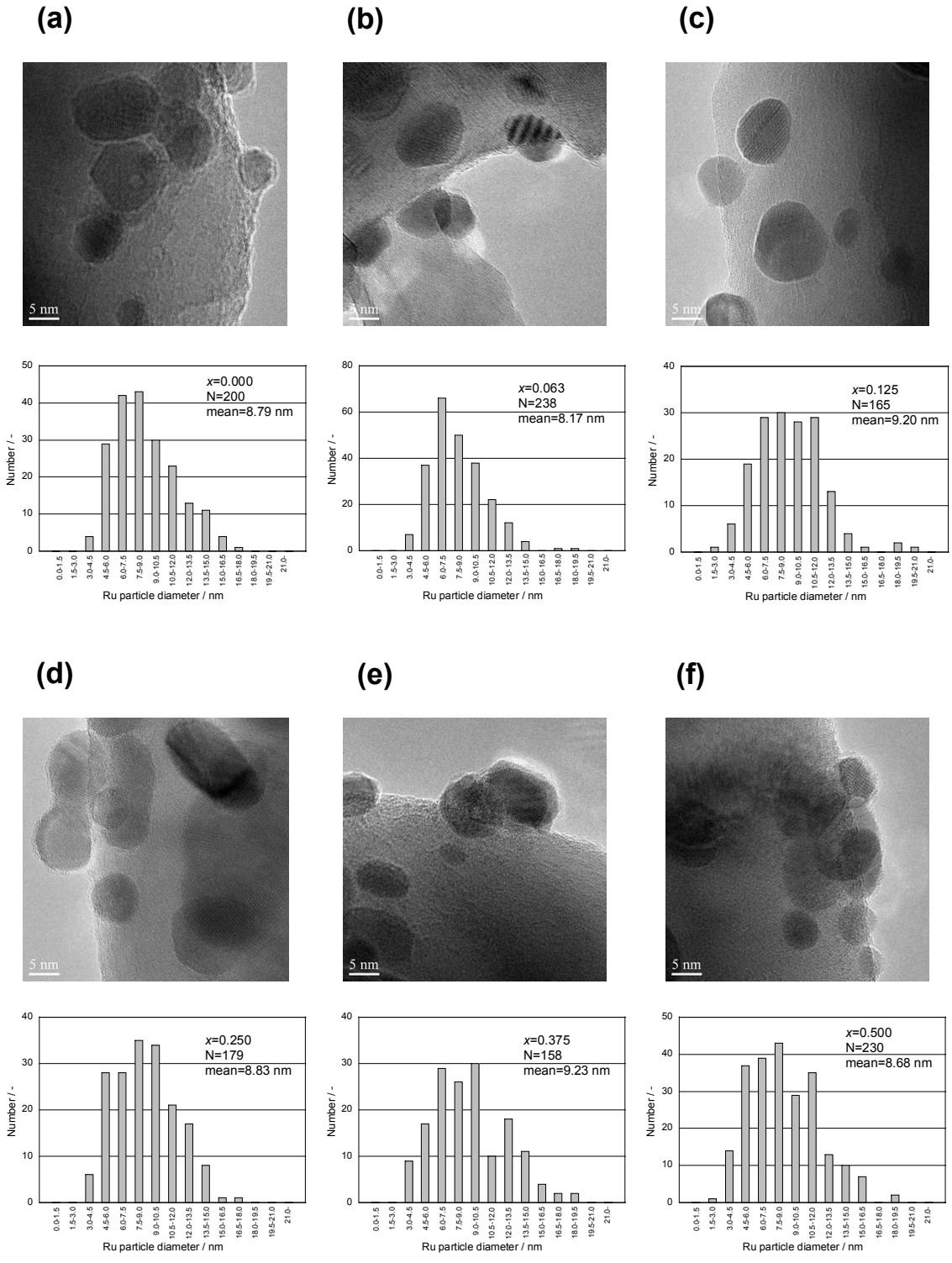

Figure S11 FE-TEM images and the obtained histograms of the 5wt%Ru/$Sr_{1-x}Ba_xZrO_3$ catalysts for (a) x=0.000, (b) x=0.063, (c) x=0.125, (d) x=0.250 (e) x=0.375, and (f) x=0.500.

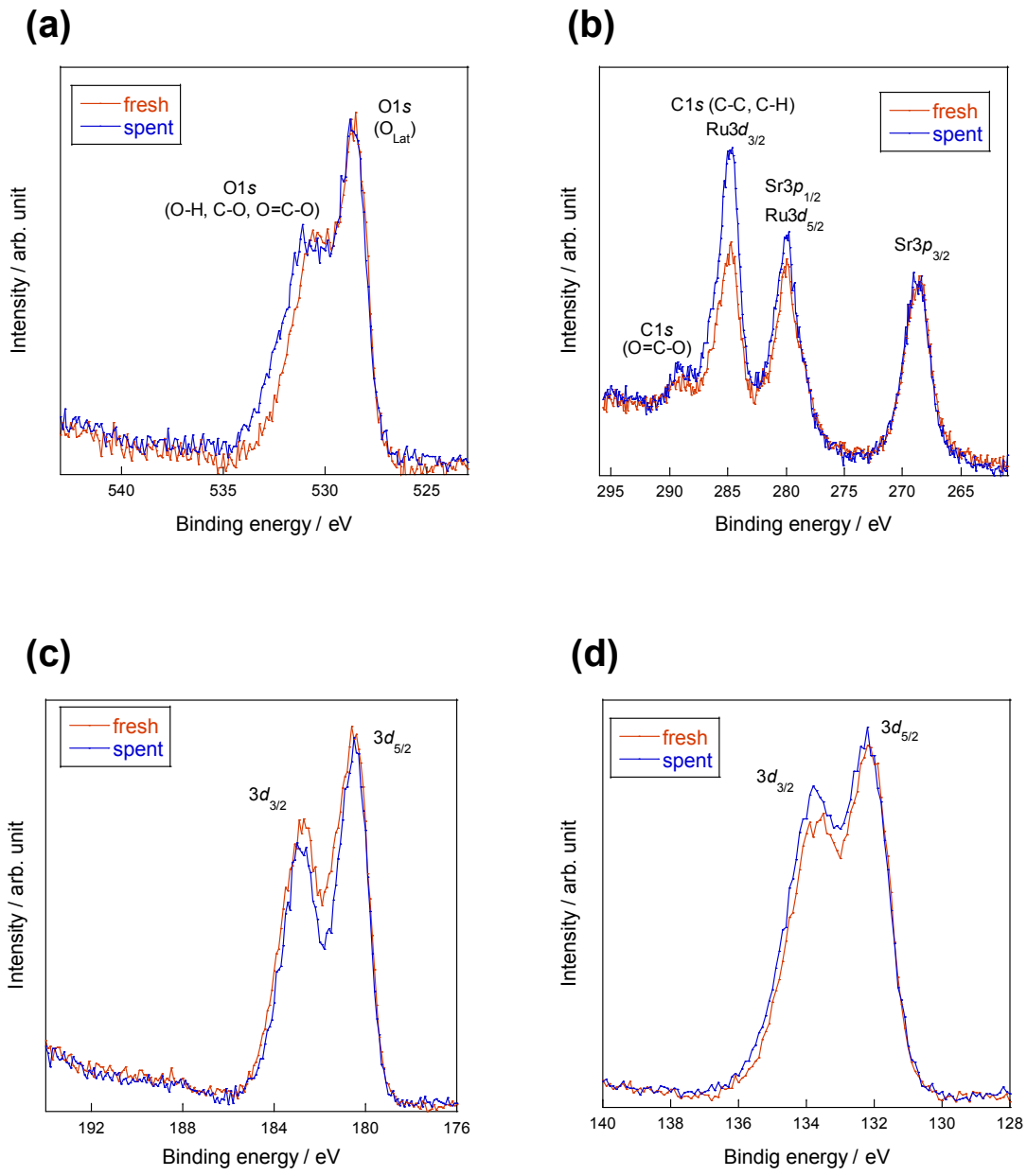

Figure S12 X-ray photoelectron spectra obtained with the fresh and the spent 5wt%Ru/$SrZrO_3$ samples, (a) O1*s*, (b) C1*s*, Ru3*d*, and Sr3*p*, (c) Zr3*d*, and (d) Sr3*d*.

Table S1 The summary for the constructed bulk and slab models of $Sr_{1-x}Ba_xZrO_3$ ($0.00 \leq x \leq 1.00$). The lattice parameters of the $BaZrO_3$ cubic oxide (*Pm-3m*) were converted using the following equation, $a' = \sqrt{2}a$, $b' = \sqrt{2}b$, and $c' = 2c$

Sr/Ba ratio (x) in $Sr_{1-x}Ba_xZrO_3$		0.00	0.25	0.50	0.75	1.00
Space group		*Pnma* (62)	*Pnma* (62)	*Imma* (74)	*I4/mcm* (139)	*Pm-3m* (221)
Crystal system		Orthorhombic	Orthorhombic	Orthorhombic	Tetragonal	Cubic
Tilt system[s12-s13]		$a^+b^-b^-$	$a^+b^-b^-$	$a^0b^-b^-$	$a^0a^0c^-$	$a^0a^0a^0$
Calculated lattice parameter	*a*	5.78	5.80	5.83	5.85	5.92
	b	5.80	5.83	5.83	5.85	5.92
	c	8.16	8.20	8.25	8.40	8.37
Exposed surface for slabs	*h*	1	-1	1	2	1
	k	1	1	1	0	0
	l	-2	-2	-2	0	1

Table S2 The summary for the H atom adsorption energies and the oxygen Bader charges over $Sr_{1-x}Ba_xZrO_3$ (x=0.00, 0.25, and 0.50) surfaces

site	Sr/Ba ratio (x) in $Sr_{1-x}Ba_xZrO_3$					
	0.00		0.25		0.50	
	Bader charge	H atom adsorption energy	Bader charge	H atom adsorption energy	Bader charge	H atom adsorption energy
-	e	eV	e	eV	e	eV
1	-0.96	-2.84	-1.22	-2.55	-0.96	-2.90
2	-0.78	-2.87	-1.13	-2.72	-0.90	-2.93
3	-0.97	-2.9	-0.86	-2.86	-0.96	-2.90
4	-0.75	-2.88	-0.75	-2.75	-0.90	-2.93
5	-0.78	-2.88	-1.14	-2.71	-0.76	-2.97
6	-0.96	-2.81	-1.22	-2.55	-0.92	-2.91
7	-0.77	-2.84	-0.73	-2.77	-0.76	-2.97
8	-0.93	-2.74	-0.87	-2.84	-0.92	-2.91
9	-0.96	-2.84	-1.22	-2.55	-0.96	-2.90
10	-0.78	-2.87	-1.13	-2.72	-0.90	-2.94
11	-0.97	-2.9	-0.86	-2.78	-0.96	-2.90
12	-0.75	-2.87	-0.75	-2.75	-0.90	-2.94
13	-0.78	-2.87	-1.14	-2.71	-0.76	-2.97
14	-0.96	-2.77	-1.22	-2.55	-0.92	-2.91
15	-0.77	-2.84	-0.83	-2.77	-0.76	-2.97
16	-0.93	-2.78	-0.87	-2.84	-0.92	-2.91
mean	-0.86	-2.84	-1.00	-2.71	-0.89	-2.93

Table S3 The summary for the quantitative OH group analysis with O1*s* XPS spectra

Sr/Ba ratio (x) in $Sr_{1-x}Ba_xZrO_3$	OH ratio	Binding energy of O_{lat}
-	-	eV
0.00	0.68	528.27
0.25	0.48	528.27
0.50	0.52	528.26

Table S4 NH_3 synthesis rate over 5wt%Ru/$SrZrO_3$ in the electric field (0.1 MPa, 6.0 mA)

Furnace temperature K	Catalyst bed temperature K	Imposed current mA	Response voltage kV	NH_3 synthesis rate $\mu mol\ g^{-1}\ h^{-1}$
R.T.	496.2	6.0	0.357	746.3
R.T.	495.2	6.0	0.383	676.8
R.T.	498.3	6.0	0.382	699.4
R.T.	487.2	6.0	0.377	652.4
R.T.	483.7	6.0	0.371	642.8
R.T.	470.7	6.0	0.337	825.2
R.T.	467.8	6.0	0.378	784.8
R.T.	460.1	6.0	0.348	759.1
373	515.2	6.0	0.323	744.0
423	535.2	6.0	0.344	686.4
473	570.5	6.0	0.289	837.4
573	641.9	6.0	0.245	1730.6

Table S5 NH_3 synthesis rate over 5wt%Ru/$Sr_{0.937}Ba_{0.063}ZrO_3$ in the electric field (0.1 MPa, 6.0 mA)

Furnace temperature	Catalyst bed temperature	Imposed current	Response voltage	NH_3 synthesis rate
K	K	mA	kV	μmol g^{-1} h^{-1}
R.T.	493.2	6.0	0.405	1081.3
R.T.	492.0	6.0	0.391	1100.3
R.T.	485.8	6.0	0.403	1079.0
R.T.	480.7	6.0	0.360	1130.8
R.T.	496.7	6.0	0.440	1189.7
R.T.	471.3	6.0	0.370	1083.6
R.T.	457.7	6.0	0.391	1054.5
R.T.	494.8	6.0	0.429	1151.8
373	500.2	6.0	0.359	1096.0
423	533.8	6.0	0.333	1215.9
473	569.4	6.0	0.319	1479.8
573	635.7	6.0	0.235	3584.2

Table S6 NH_3 synthesis rate over 5wt%Ru/$Sr_{0.875}Ba_{0.125}ZrO_3$ in the electric field (0.1 MPa, 6.0 mA)

Furnace temperature	Catalyst bed temperature	Imposed current	Response voltage	NH_3 synthesis rate
K	K	mA	kV	μmol g^{-1} h^{-1}
R.T.	488.5	6.0	0.391	1222.9
R.T.	480.2	6.0	0.365	1023.4
R.T.	487.2	6.0	0.402	1138.3
R.T.	480.0	6.0	0.351	1117.3
R.T.	484.6	6.0	0.400	1160.8
R.T.	500.9	6.0	0.401	1224.5
R.T.	499.8	6.0	0.389	1201.7
R.T.	499.1	6.0	0.399	1249.4
373	507.9	6.0	0.368	1197.0
423	545.1	6.0	0.346	1432.8
473	571.0	6.0	0.326	1676.2
573	646.4	6.0	0.284	3937.7

Table S7 NH_3 synthesis rate over 5wt%Ru/$Sr_{0.750}Ba_{0.250}ZrO_3$ in the electric field (0.1 MPa, 6.0 mA)

Furnace temperature	Catalyst bed temperature	Imposed current	Response voltage	NH_3 synthesis rate
K	K	mA	kV	μmol g^{-1} h^{-1}
R.T.	498.9	6.0	0.422	1009.8
R.T.	497.4	6.0	0.409	981.5
R.T.	500.0	6.0	0.439	999.5
R.T.	505.1	6.0	0.451	1070.5
R.T.	506.0	6.0	0.456	1106.4
R.T.	490.6	6.0	0.434	1094.9
R.T.	482.6	6.0	0.440	973.8
R.T.	481.1	6.0	0.410	935.4
373	524.2	6.0	0.360	1035.6
423	545.2	6.0	0.344	1161.5
473	573.6	6.0	0.307	1336.9
573	633.7	6.0	0.205	2857.7

Table S8 NH_3 synthesis rate over 5wt%Ru/$Sr_{0.625}Ba_{0.375}ZrO_3$ in the electric field (0.1 MPa, 6.0 mA)

Furnace temperature	Catalyst bed temperature	Imposed current	Response voltage	NH_3 synthesis rate
K	K	mA	kV	μmol g^{-1} h^{-1}
R.T.	479.7	6.0	0.403	967.7
R.T.	478.3	6.0	0.393	733.1
R.T.	479.9	6.0	0.393	708.6
R.T.	481.0	6.0	0.388	697.5
R.T.	482.0	6.0	0.405	866.9
R.T.	484.4	6.0	0.397	889.3
R.T.	497.4	6.0	0.388	692.9
R.T.	498.3	6.0	0.384	842.9
373	507.5	6.0	0.365	670.9
423	531.4	6.0	0.284	932.2
473	554.9	6.0	0.278	1039.4
573	634.7	6.0	0.244	2509.6

Table S9 NH_3 synthesis rate over 5wt%Ru/$Sr_{0.500}Ba_{0.500}ZrO_3$ in the electric field (0.1 MPa, 6.0 mA)

Furnace temperature	Catalyst bed temperature	Imposed current	Response voltage	NH_3 synthesis rate
K	K	mA	kV	μmol g^{-1} h^{-1}
R.T.	490.4	6.0	0.391	819.1
R.T.	484.8	6.0	0.374	791.9
R.T.	484.7	6.0	0.368	750.0
R.T.	488.2	6.0	0.379	756.2
R.T.	487.8	6.0	0.382	762.8
R.T.	467.1	6.0	0.374	1044.7
R.T.	452.9	6.0	0.378	908.8
R.T.	480.5	6.0	0.444	1092.5
373	515.3	6.0	0.378	942.3
423	523.4	6.0	0.303	999.2
473	561.8	6.0	0.287	1198.3
573	641.9	6.0	0.245	3480.4

Table S10 Specific surface areas of the fresh and the spent 5wt%Ru/$Sr_{1-x}Ba_xZrO_3$ ($0.000 \leq x \leq 0.500$) catalysts

Sr/Ba ratio (x) in 5wt%Ru/$Sr_{1-x}Ba_xZrO_3$	Specific surface are (BET method)	
	fresh	spent
-	$m^2\ g^{-1}$	$m^2\ g^{-1}$
0.000	6.11	6.67
0.063	6.46	7.11
0.125	7.21	7.59
0.250	7.31	6.79
0.375	7.88	7.87
0.500	8.05	9.36